Draft version March 19, 2021
Typeset using LaTeX **twocolumn** style in AASTeX63

arXiv:2103.06548v2 [astro-ph.HE] 18 Mar 2021

Fast Blue Optical Transients due to Circumstellar Interaction and the Mysterious Supernova SN 2018gep

Shing-Chi Leung,[1] Jim Fuller,[1] and Ken'ichi Nomoto[2]

[1] *TAPIR, Walter Burke Institute for Theoretical Physics, Mailcode 350-17, Caltech, Pasadena, CA 91125, USA*
[2] *Kavli Institute for the Physics and Mathematics of the Universe (WPI), The University of Tokyo Institutes for Advanced Study, The University of Tokyo, Kashiwa, Chiba 277-8583, Japan*

(Dated: March 19, 2021; Received 10 March 2021)

Submitted to Astrophysical Journal

ABSTRACT

The discovery of SN 2018gep (ZTF18abukavn) challenged our understanding of the late-phase evolution of massive stars and their supernovae (SNe). The fast rise in luminosity of this SN (spectroscopically classified as a broad-lined Type Ic SN), indicates that the ejecta interacts with a dense circumstellar medium (CSM), while an additional energy source such as ^{56}Ni-decay is required to explain the late-time light curve. These features hint at the explosion of a massive star with pre-supernova mass-loss. In this work, we examine the physical origins of rapidly evolving astrophysical transients like SN 2018gep. We investigate the wave-driven mass-loss mechanism and how it depends on model parameters such as progenitor mass and deposition energy, searching for stellar progenitor models that can reproduce the observational data. A model with an ejecta mass $\sim 2\,M_\odot$, explosion energy $\sim 10^{52}$ erg, a circumstellar medium of mass $\sim 0.3\,M_\odot$ and radius $\sim 1000\,R_\odot$, and a ^{56}Ni mass of $\sim 0.3\,M_\odot$ provides a good fit to the bolometric light curve. We also examine how interaction-powered light curves depend more generally on these parameters, and how ejecta velocities can help break degeneracies. We find both wave-driven mass-loss and mass ejection via pulsational pair-instability can plausibly create the dense CSM in SN 2018gep, but we favor the latter possibility.

Keywords: Supernovae(1668) – Supernova dynamics(1664) – Concept: Radiative transfer – Concept: Light curves – Stellar pulsations(1625)

1. INTRODUCTION

1.1. *Shock Interaction Mechanism*

The shock-interaction model (Chevalier 1982) is one of the proposed models (e.g., Woosley et al. 2007; Moriya et al. 2013; Chatzopoulos et al. 2013; Morozova et al. 2015; Sorokina et al. 2016; Blinnikov 2017; Kasen 2017; Smith 2017; Moriya et al. 2018) to explain the diversity of highly luminous supernovae (SNe), in parallel with magnetar-powered SNe (Maeda et al. 2007; Woosley 2010; Kasen & Bildsten 2010; Kasen et al. 2016), accretion-powered SNe (Dexter & Kasen 2013; Wang et al. 2018) and pair-instability SNe (Kasen et al. 2011; Gilmer et al. 2017).

Corresponding author: Shing-Chi Leung
scleung@caltech.edu

Shock-interaction occurs when the rapidly expanding stellar ejecta collides with the quasi-static CSM. The ejecta drives a shock through the CSM, which converts the ejecta kinetic energy into thermal energy, leading to the bright event observed. The model has been applied to recent super-luminous SNe such as SN 2008gy (Woosley et al. 2007), SN 2007bi, SN 2010gx & PTF09cnd (Sorokina et al. 2016), iPTF14hls (Woosley 2018), PTF12dam (Tolstov et al. 2017), AT2018cow (Leung et al. 2020b) and PS15dpn (Wang & Li 2020).

To explain the origin of the CSM, a number of mechanisms can trigger greatly enhanced mass loss prior to the final stellar explosion, including common envelope-triggered mass loss (Chevalier 2012; Schrøder et al. 2020), pulsation-induced mass-loss in pulsational pair-instability SNe (Umeda & Nomoto 2003; Woosley 2017; Marchant et al. 2019; Leung et al. 2019, 2020a; Woosley 2019; Renzo et al. 2020), enhanced stellar wind

in super-AGB stars (Jones et al. 2013; Moriya et al. 2014; Nomoto & Leung 2017; Tolstov et al. 2019; Leung & Nomoto 2019) and wave-driven mass-loss (Quataert & Shiode 2012; Shiode & Quataert 2014; Fuller 2017; Fuller & Ro 2018; Ouchi & Maeda 2019; Leung & Fuller 2020; Kuriyama & Shigeyama 2020).

Pulsation-induced mass loss relies on the electron-positron pair-creation catastrophe (Barkat et al. 1967) which happens in very massive stars ($\sim 80 - 140\,M_\odot$) (Umeda & Nomoto 2002; Heger & Woosley 2002; Ohkubo et al. 2009; Hirschi 2017; Yoshida et al. 2016). These radiation-dominated stars lose core pressure support from photons during their conversion into electron-positron pairs. The contraction of the star's core becomes dynamical, triggering explosive burning of C and O. The excess energy generation makes the core bounce, driving a shock through the envelope that ejects mass from the surface. The star can experience several mass-loss events, depending on the available carbon and oxygen in the core (Woosley 2017; Marchant et al. 2019; Leung et al. 2019; Woosley 2019; Renzo et al. 2020).

In Leung et al. (2020b), we explored the possibility of applying the pulsation-induced mass-loss model to explain the rapid transient AT2018cow. Like SN 2018gep, AT2018cow is also classified as a "Fast Bright Optical Transient" (FBOT). That work, together with Tolstov et al. (2017), suggests that PPISNe provides the flexibility to span the wide diversity of transient objects from FBOT to super-luminous SNe. However, the unusually rapid transient in SN 2018gep leads to speculation whether other mass loss mechanisms are necessary to explain the optical signals of this object.

Wave-driven mass loss (Quataert & Shiode 2012; Shiode & Quataert 2014; Fuller 2017; Fuller & Ro 2018; Wu & Fuller 2020) relies on the vigorous convective motions in the massive star's core during its late-phase nuclear burning (e.g., carbon-burning and later advanced burning stages). This in turns excites internal gravity waves that propagate through the radiative core, where some of the wave energy is transmitted into the envelope via acoustic waves. When the waves reach the surface where the density gradient is large, they develop into weak shocks that dissipate and deposit their energy in the surroundings. Even though only a small fraction of the wave energy is leaked to the envelope, it can be sufficient to eject a substantial amount of mass.

1.2. *SN2018gep as a Rapid Transient*

SN 2018gep (ZTF18abukavn) is a supernova discovered by the Zwicky Transient Factory (ZTF) (Bellm et al. 2019; Graham et al. 2019), first analyzed by Ho et al. (2019) and later by (Pritchard et al. 2020). This object has photometric and spectroscopic features similar to some other recent rapid transients, such as AT2018cow (Smartt et al. 2018; Prentice et al. 2018; Perley et al. 2019; Margutti et al. 2019) and iPTF16asu (Wang et al. 2019; Whitesides et al. 2017). SN2018gep is remarkable for its very early detection by ZTF and its proximity at ~ 143 Mpc from the Earth, which allowed for detailed follow-up observations.

Among all rapid transients, SN 2018gep has a fast rise time of 0.5 – 3 days (Ho et al. 2019) until it reached a large peak luminosity of 3×10^{44} erg s^{-1}. Its low-mass and compact host galaxy has a metallicity only one-fifth of solar metallicity. The surface temperature of the transient at its peak of ~ 40000 K is the highest among all striped-envelope SNe. The upper limits of detection by high energy bands (X-ray and gamma-ray) and the radio band have led to speculations that this explosion experiences shock-interaction between the explosion ejecta and the circumstellar medium (CSM).

1.3. *Outline*

In Section 2, we perform hydrodynamical modeling of mass loss from helium star SN progenitors due to wave heating, predicting the resulting CSM structure at the time of explosion. In Section 3 we compare the CSM properties from our wave-driven mass loss models to radiative transfer models of this work and those in Ho et al. (2019). We also include PPISN models from the literature to contrast the corresponding CSM properties of this class of stars. In Section 4 we present radiative transfer modelling and an explosion parameter search to fit the bolometric light curve of SN 2018gep. We then discuss the robustness of our results in Section 5, examining possible degeneracies, comparing to other models of SN 2018gep, and discussing the physical origins of this event. Finally we summarize the findings of this work and highlight our interpretation of SN 2018gep.

2. WAVE-DRIVEN MASS LOSS

2.1. *General Modeling Method*

To investigate wave-driven mass loss and to construct pre-collapse models for radiative transfer modeling, we use the one-dimensional stellar evolution code MESA (Paxton et al. 2011, 2013, 2015, 2017), version 8118. We model stars with initial masses 20 – 80 $M_\odot$, which correspond to He cores with masses ~ 5 – 40 $M_\odot$ (Hirschi 2017; Woosley 2017). The final mass before collapse, even without dynamical mass loss, depends strongly on the initial metallicity due to mass loss from line-driven winds. We follow the entire stellar evolution from the

Table 1. The initial, He-core, C-core and pre-explosion mass of the models studied in this work. We assume $Z = 0.02$ and a Dutch wind coefficient $\eta = 0.8$.

$M_{\rm ini}$ ($M_\odot$)	$M_{\rm He}$ ($M_\odot$)	$M_{\rm C}$ ($M_\odot$)	$M_{\rm exp}$ ($M_\odot$)
25	6.56	3.00	5.44
40	12.97	5.58	9.20
60	21.78	9.58	12.22

onset of core H-burning until the onset of gravitational collapse.

We consider only stripped-envelope stars in this work because this class of stars produce hydrogen-free Type Ib/c SNe like SN 2018gep. We first model a zero-age main-sequence star until hydrogen is exhausted in the core. Then we remove the H-envelope and continue the evolution. In Table 1, we list relevant masses for the progenitor models in this study. Although the ZAMS mass is the model parameter we control, we will focus on the pre-explosion mass $M_{\rm exp}$, as it determines the SN ejecta mass, along with the core evolution and hence the wave-driven mass-loss.

To investigate the process of wave-driven mass loss, we follow a scheme similar to that described in Fuller & Ro (2018). Once an oxygen-burning core has developed in the star, we terminate the simulation. We set the inner boundary at 1 $M_\odot$, interior to the carbon core outer boundary. We keep the outer carbon layer as a buffer, but in general, the mass loss is very small and the carbon layer remains unchanged.

To calculate how the wave energy is deposited in the envelope, we follow the method of Fuller & Ro (2018), in which the outgoing acoustic wave luminosity $L_{\rm wave}$ decreases as

$$\frac{dL_{\rm wave}}{dM} = -\frac{L_{\rm wave}}{M_{\rm wave,shock}} - \frac{L_{\rm wave}}{M_{\rm wave,diff}}, \quad (1)$$

The local value of $dL_{\rm wave}/dM$ is the deposited energy per unit mass within the star. Above, $M_{\rm wave,shock}$ and $M_{\rm wave,diff}$ are the expected damping mass by shock heating and radiative diffusion, given by:

$$M_{\rm wave,shock} = 3\pi\frac{\gamma+1}{\omega}c_s^2\left(\frac{L_{\rm max}^3}{L_{\rm wave}}\right)^{1/2}, \quad (2)$$

$$M_{\rm wave,diff} = \frac{2L_{\rm max}}{\omega^2 K}, \quad (3)$$

where γ, c_s^2 and K are the adiabatic index, sound speed squared and thermal diffusivity (Fuller 2017). $L_{\rm max} = 2\pi\rho r^2 c_s^3$ is the maximum energy transportable by linear acoustic waves and ω is the wave frequency. The wave frequencies excited by convection are typically in the range $\omega = 10^{-2} - 10^{-3}$ s^{-1} and are a model parameter in this work. Additionally, the outflowing matter can expand with a super-sonic velocity, stretching the acoustic wavelength and increasing the value of $M_{\rm wave,diff}$ and $M_{\rm wave,shock}$ as described in Fuller & Ro (2018).

Similar to our previous work (Leung & Fuller 2020), when we model the envelope dynamics, we treat the duration of energy deposition as a parameter. This allows us to model the resulting interaction-powered light curve as a function of both the wave energy deposition and its duration, but we note that the two parameters are linked when modeling the inner core evolution of the star, as investigated in Shiode & Quataert (2014) and Wu & Fuller (2020). We retain all of the ejected CSM on our model grids because the typical timescale from the onset of O-burning to the final collapse is $\sim$0.1 year, and the corresponding CSM radius is less than 10^4 $R_\odot$.

2.2. *Dependence on Deposition Duration*

We first study how the CSM properties depend on the energy deposition duration. We consider a 5.4 $M_\odot$ He star with $Z = 0.02$. In the energy deposition phase, we deposit a total of 6×10^{47} erg energy in the envelope, a value near the upper end of the envelope wave energy deposition range found in Wu & Fuller (2020). The duration, which depends on the exact duration of O-burning, is treated as a free parameter from 0.05 to 1.35 year, which covers the typical O-burning duration for a wide range of stellar mass. In Figure 1, we plot the hydrodynamical profiles of these models at the end of the simulations.

The density profile shows a generally smooth structure with radial dependence similar to (though slightly steeper than) that for a steady wind, $\rho \propto r^{-2}$. The density profile is also punctuated by spikes associated with internal shocks, which arise due to the uneven energy deposition (and hence uneven outflow velocity) at early times. Near its outer edge, the CSM has a typical density of 10^{-10} – 10^{-13} g cm^{-3}. The temperature also falls rapidly with radius, except in the outermost optically thin layers where it is constant. The ejecta moves away from the core with a typical velocity of $\sim 3-5\times10^7$ cm s^{-1}, but with an exception for the longest energy deposition model ($t_{\rm dep} = 1.35$ year), in which the expansion of the star is quasi-hydrostatic. The escape velocity at large radii is about 3×10^6 cm s^{-1}, confirming that the ejected matter can successfully escape from the gravity of the star.

The luminosity profile demonstrates how the star distributes the deposited wave energy. In the bound portion of the star, the luminosity is constant at $\approx 10^5$ $L_\odot$. Across the energy deposition zone, the stellar luminos-

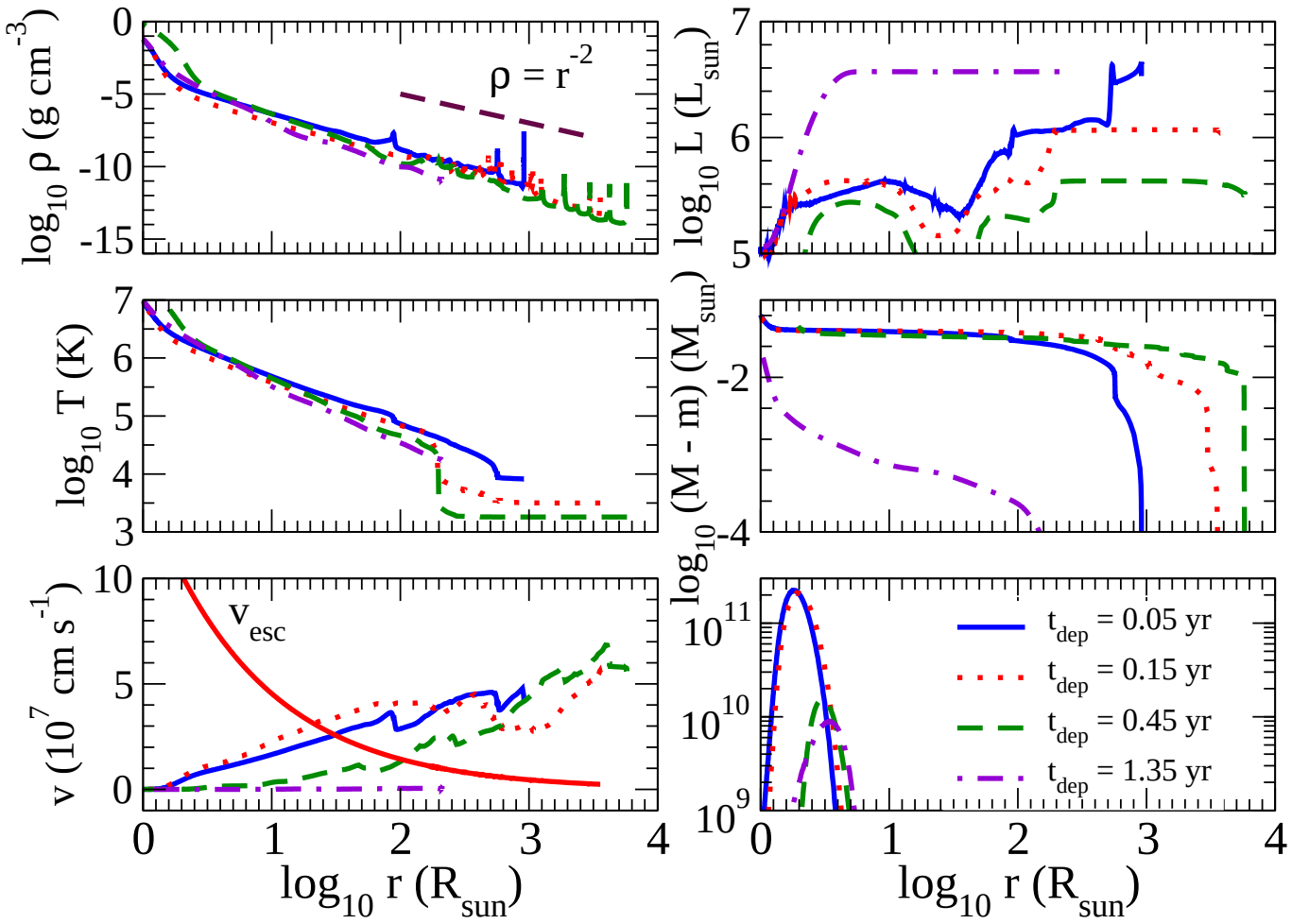

Figure 1. The hydrodynamic profile of stellar models at the end of the wave heating simulations including the density (top left), temperature (middle left), velocity (bottom left), luminosity (top right), external mass (middle right) and local energy deposition rate in units of erg s^{-1} (bottom right). The progenitor model is a helium core with a pre-explosion mass $M_{\rm exp} = 5.4\ M_\odot$ at $Z = 0.02$, and a deposited energy of 6×10^{47} erg over a time scale before core-collapse of $t_{\rm dep} = 0.05$ (blue solid line), 0.15 (red dotted line), 0.45 (green dashed line) and 1.35 year (purple dot-dashed line) respectively. In the bottom left plot, we include the escape velocity using the model with $t_{\rm dep} = 0.15$ year.

ity quickly rises by one to two orders of magnitude, but is smaller than the total wave heating rate. This shows that much of the wave energy is used to unbind material (i.e., increase its gravitational potential energy) and convert it to kinetic energy of the outflow. An exception is the model with $t_{\rm dep} = 1.35\,$yr, in which matter is not efficiently ejected and most of the wave energy is radiated from the star. Note also that the star's luminosity can decrease or increase within the outflowing material, the latter occurring as kinetic energy from colliding shells is converted into heat that is radiated outward.

The external mass coordinate profile of $M - m$ shows the radial dependence of the ejected mass, with most of the mass located in the outer part of the CSM where the $M-m$ profiles turn over between roughly $300-3000\,R_\odot$. We see that the ejected mass is a few hundredths of a solar mass for all but the longest energy deposition time scale.

We next examine the energy deposition profile when the simulation ends, recalling that the energy deposition zone is time-dependent. The energy deposition zone moves towards to the stellar core as the heated zone expands. We also see that the waves damp at a smaller radius when $t_{\rm dep}$ becomes small, because the corresponding $L_{\rm wave} = E_{\rm dep}/t_{\rm dep}$ becomes large, so that the acoustic waves develop into weak shocks at a higher density, and thus at a smaller radius. The peak of the heat deposition also occurs near the sonic point of the outflow, i.e., near the boundary between the nearly hydrostatic star and the outflowing CSM.

2.3. *Dependence on Deposition Energy*

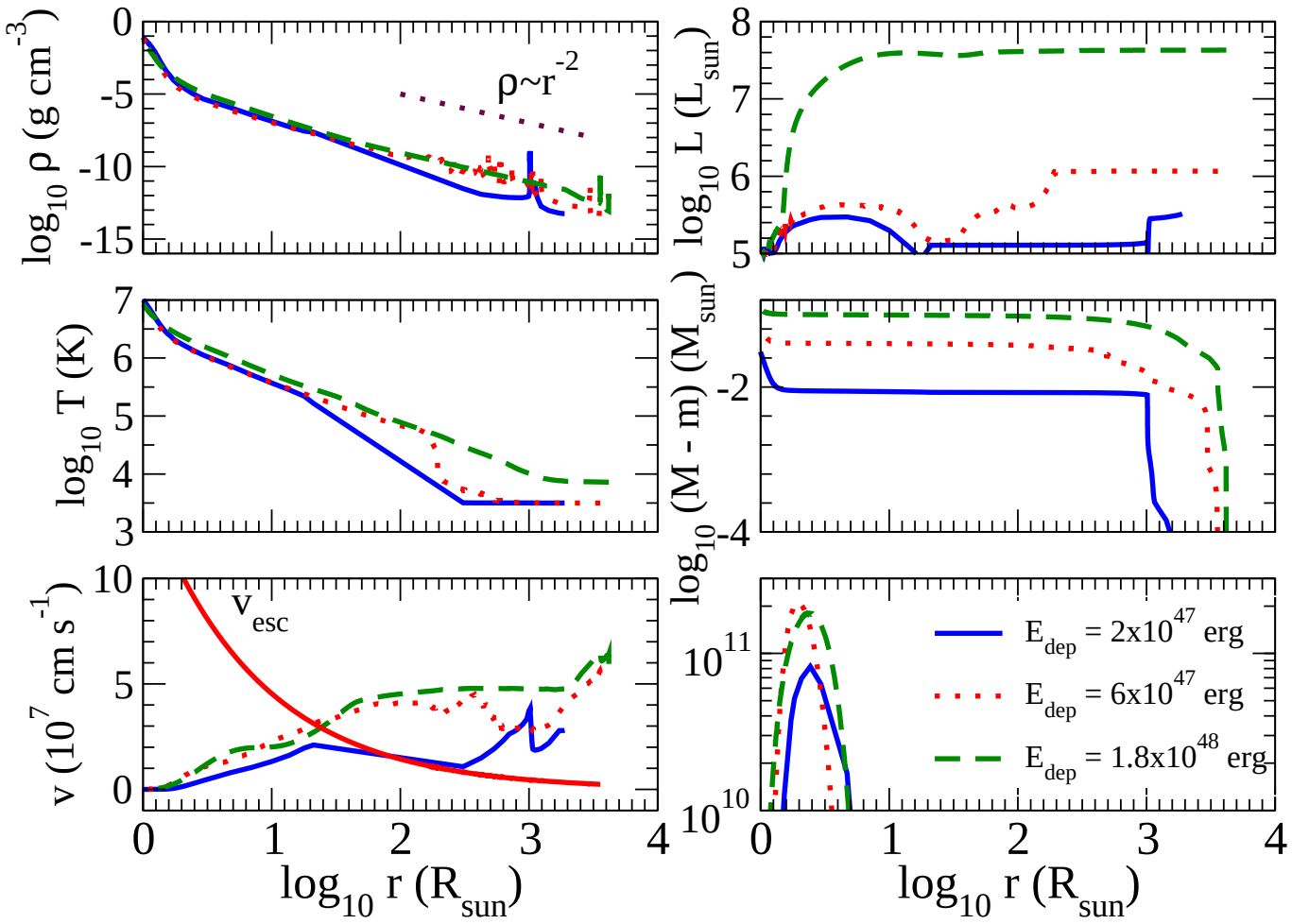

Figure 2. Similar to Figure 1 but for models with a total energy deposition of 2×10^{47}, 6×10^{47} and 1.8×10^{48} erg respectively. A model with a pre-explosion mass of 5.4 $M_\odot$ and a duration of 0.15 year of energy deposition are used during the simulation. The escape velocity in the bottom left plot used the data from the model with $E_{\rm dep} = 6\times10^{47}$ erg.

We next compare how the total energy deposition changes the CSM profile of the 5.4 $M_\odot$ model, fixing the deposition duration at 0.15 year. In general, the net energy deposition is determined by the core structure and evolution, and Wu & Fuller (2020) find typical energies of a few $\times10^{47}$ erg for a wide number of models, with many massive star models in the range $10^{47} - 10^{48}$ erg. Hence, we consider total energy depositions of 2×10^{47} erg, 6×10^{47} erg, and 1.8×10^{48}.

Figure 2 shows that the total energy deposition is another primary factor affecting the CSM. While the density and temperature profiles are fairly similar between the models, the ejecta mass varies by about an order of magnitude, with the model with $E_{\rm dep} = 1.8\times10^{48}$ erg ejecting about 0.063 $M_\odot$, whereas the model with 2×10^{47} erg ejects about 0.009 $M_\odot$. The ejected mass scales approximately linearly with the injected energy. The CSM also extends to slightly larger radii for larger energy deposition. The ejecta velocity shows only minor variations between the models, with the low-energy model exhibiting slightly larger velocity at the end of the simulation. The luminosity also does not monotonically change with $E_{\rm dep}$, with a much higher luminosity for the largest $E_{\rm dep}$ model.

2.4. *Dependence on Progenitor Mass*

We proceed to examine how the wave heating process affects helium stars of different mass. A higher progenitor mass leads to a more compact core with a smaller radius during oxygen burning, which results in an envelope of higher binding energy. In Figure 3 we compare models with a pre-explosion mass of 5.4, 9.2 and 12.2 $M_\odot$ (corresponding to ZAMS models of 25, 40 and 60 $M_\odot$ respectively, see Table 1). For ease of interpretation, we assume a fixed energy deposition of 6×10^{47} erg for a duration of 0.15 year, similar to the O-burning duration of a 40 $M_\odot$ star.

In Figure 3, we plot the hydrodynamical profiles of these models at the end of these simulations. Higher

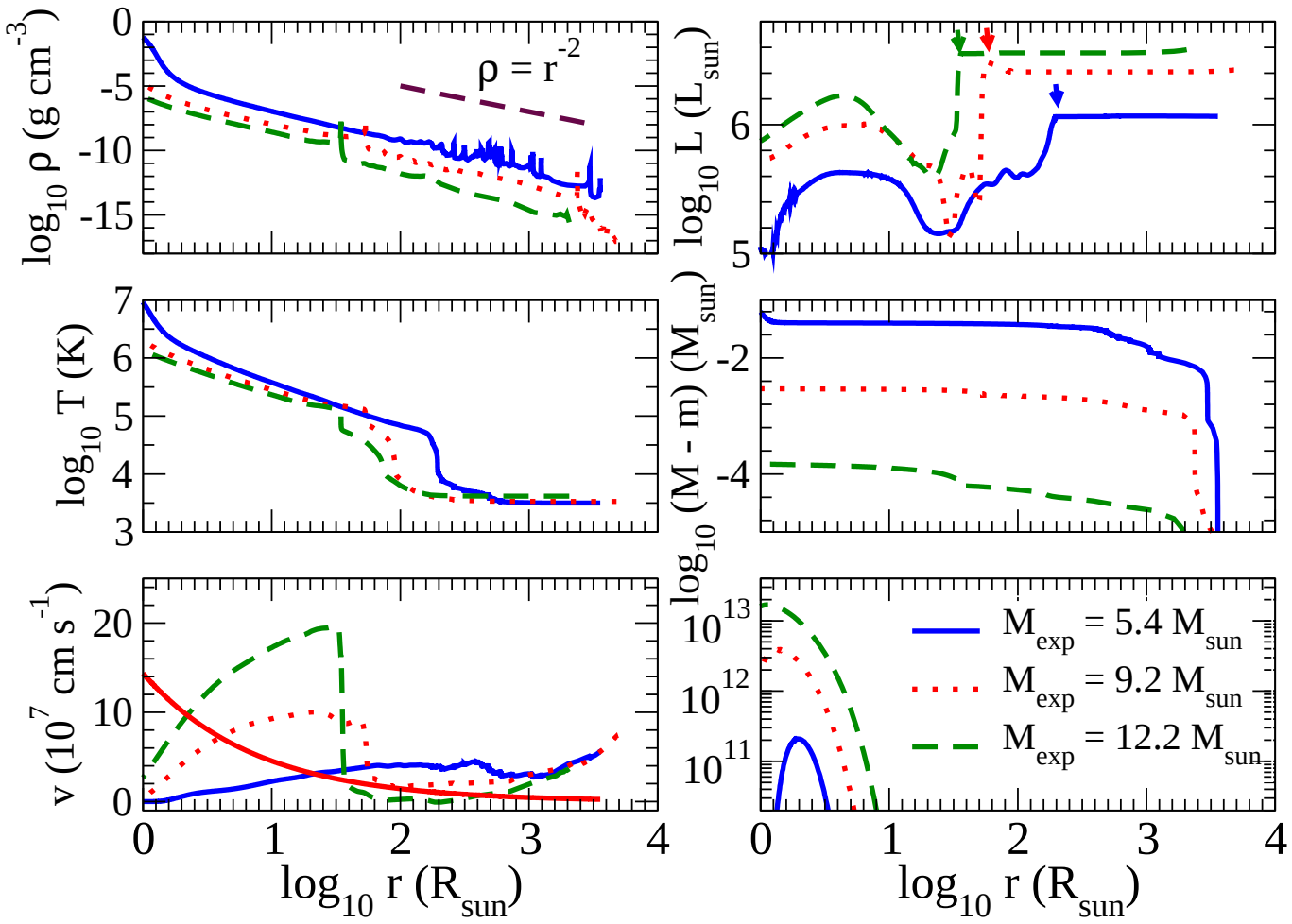

Figure 3. Similar to Figure 1 but for models with a pre-explosion mass of 5.4 (blue solid line), 9.2 (red dotted line) and 12.2 $M_\odot$ (green dashed line) respectively. An energy of 6×10^{47} erg over a duration of 0.15 year is deposited during the simulation. In the top right panel, we add the arrows to indicate the formal photosphere ($\tau = 2/3$) radius. In the bottom left plot, the escape velocity (solid red line) corresponds to that of the model with $M_{\rm exp} = 5.44\ M_\odot$.

stellar mass leads to a much lower amount of mass being ejected, from more than $10^{-2}\ M_\odot$ in the 5.4 $M_\odot$ model, down to about $10^{-4}\ M_\odot$ in the 12.2 $M_\odot$ model. The outermost layers of the CSM extend to a few thousand solar radii in each case. Again the density profile falls off slightly steeper than r^{-2}, and the temperature profile flattens at a temperature of $T \approx 6000$ K in the optically thin outer regions of the ejecta. The luminosity of the models is about ten to a hundred times of the original luminosity and increases with $M_{\rm exp}$.

3. PHYSICAL MODELS OF SN 2018GEP

As discussed in the introduction, pulsation-driven mass loss is a well studied mechanism for explaining a wide range of observed CSM and its shock-interaction implied in supernova light curves. In this section, we compare the CSM properties produced by the wave-driven mass-loss models and PPISN models. We also study how the two models compare to the CSM constraints derived from radiative transfer modeling of SN 2018gep in this work (See Section 4 for details) and in Ho et al. (2019).

We compare the associated mass loss of the two models in Figure 4, where we plot the total ejected mass against the pre-explosion mass of the star. Data for PPISN models come from prior results in the literature (Renzo et al. 2020; Leung et al. 2019). We can see two distinctive clusters in the figures. On the lower mass side (wave-driven mass loss), there is a clear trend in which the ejected mass decreases with pre-explosion mass, as discussed in the previous section. For the PPISN models on the right hand side, we see a clear rising trend in which ejecta mass typically increases with pre-explosion mass. We also see the two sets of PPISN models mostly agree with each other. In both regimes, the trends are accompanied by scatter because the exact amount of mass loss is coupled to highly nonlinear or uncertain

factors, including the temperature-sensitive carbon- and oxygen burning, or the amount of wave energy transport.

The gap between the two clusters of models exists because we do not consider low metallicity models ($Z < 0.002$) for our wave-driven mass loss calculations, so mass loss from line-driven winds prevents the formation of pre-explosion masses greater than $\sim 20\,M_\odot$. While lower metallicity models can produce pre-explosion masses above this limit, we do not expect wave-driven mass loss to play an important role in CSM formation for those stellar models, based on the trend in this work. Furthermore, until the pre-explosion mass approaches $35\,M_\odot$, the models are not massive enough to trigger pair-creation instability, thus having no mass loss by pulsation.

We also plot two horizontal lines in the figure, corresponding to the CSM masses derived from the radiative transfer models of SN 2018gep in Ho et al. (2019) and in this work. The wave-driven mass loss model cannot match the higher $M_{\rm CSM}$ value derived from our radiative transfer models, but it can match the value inferred from Ho et al. (2019) in progenitors with a mass $4 - 10\ M_\odot$. On the other side, both possible CSM masses can be explained by pulsation-induced mass-loss. The smaller CSM mass from Ho et al. (2019) can be explained by PPISN models with $M \sim 35\,M_\odot$; while our higher inferred CSM mass matches models with a pre-explosion mass $\sim 40\ M_\odot$.

In the middle panel of Figure 4, we show the time delay between the mass ejection and the onset of core-collapse for the same sets of models. For our wave-driven mass loss models, the energy deposition time is a model parameter as discussed in the previous section. For pulsation driven mass loss, the time delay is defined as the time between the first pulse and core-collapse. The PPISNe have a wide range of time delays which span from $\sim 10^{-5} - 10^{1}$ year. We also plot the observed time delay inferred from pre-explosion imaging of the progenitor of SN 2018gep in Ho et al. (2019), which revealed an outburst roughly 15 days (0.04 years) before the final explosion. Many of the PPISN models in Renzo et al. (2020) are near the observed time delay of $\sim$0.04 yr for SN 2018gep, but this time delay is also similar to that expected for many wave-driven mass loss models.

In the bottom panel of Figure 4, we plot the characteristic CSM radius for our models and the PPISN models of Renzo et al. (2020). We define the characteristic CSM radius as the mass-averaged radius of material which has a positive energy. For the PPISN models, we estimate $R_{\rm CSM} =< v > \Delta t$, where Δt is the same time delay used in the middle panel, and $< v >$ is the mass-averaged ejecta velocity from Renzo et al. (2020).

The wave-driven models do not show an obvious trend in the CSM radius, though it is possible that more realistic models (which self-consistently calculate wave energy transport as a function of time) would exhibit a trend. In any case, they span a range in CSM radius from roughly $10^2 - 10^4\,R_\odot$. This range includes the estimated CSM radius from radiative transfer modeling of $R_{\rm CSM} \sim 10^3\,R_\odot$ in this work (again see Section 4), and $R_{\rm CSM} \sim 4000\,R_\odot$ from Ho et al. (2019). On the other hand, the PPISN models predict a wide range of CSM radii from roughly $10 - 10^5\ R_\odot$. They also cover both the CSM radius suggested in this work and in Ho et al. (2019).

By combining all three plots, we determine the most likely progenitor model of SN 2018gep. The wave-driven models can match the ejecta mass and time delay from Ho et al. (2019), but they struggle to match the larger $R_{\rm CSM}$ from that work. Additionally, the wave-driven mass loss models cannot match the larger $M_{\rm CSM}$ inferred from our radiative transfer models in Section 4.

Most PPISN models exceed the CSM mass found from Ho et al. (2019), but they can match the larger CSM mass from our radiative transfer models. The time delay can also be comparable with that observed. However, the PPISN models which match the CSM mass from this work typically exceed the CSM radius from this work by a factor of a few. Those that match the CSM mass from Ho et al. (2019) have smaller CSM radii than that inferred from Ho et al. (2019), and their outburst times are shorter than that observed. In conclusion, there are no individual PPISN models which perfectly match the CSM mass, radius, and pre-explosion time, but there are several at masses of $37 - 44\,M_\odot$ that are within a factor of a few of the inferred values.

Ho et al. (2019) also found an ejecta mass of $\sim 8\ M_\odot$ from modeling the late-time light curve, implying a pre-explosion mass near $10\,M_\odot$ if a neutron star is formed during the explosion. Such progenitors struggle to eject enough CSM mass by the wave-driven mass loss mechanism, unless we consider models with an optimistic amount of deposited energy ($\gtrsim 10^{48}$ erg). However, the inferred ejecta mass is much lower than the pre-exposion mass required for pulsation-induced mass loss. Hence, PPISN models can only match the ejecta mass if a large fraction of the progenitor mass collapses into a black hole, or if the SN ejecta is not spherically symmetric (e.g., most of the SN light arises from high-velocity bipolar lobes containing a small fraction of the ejecta mass).

4. LIGHT CURVE FITTING OF SN 2018GEP

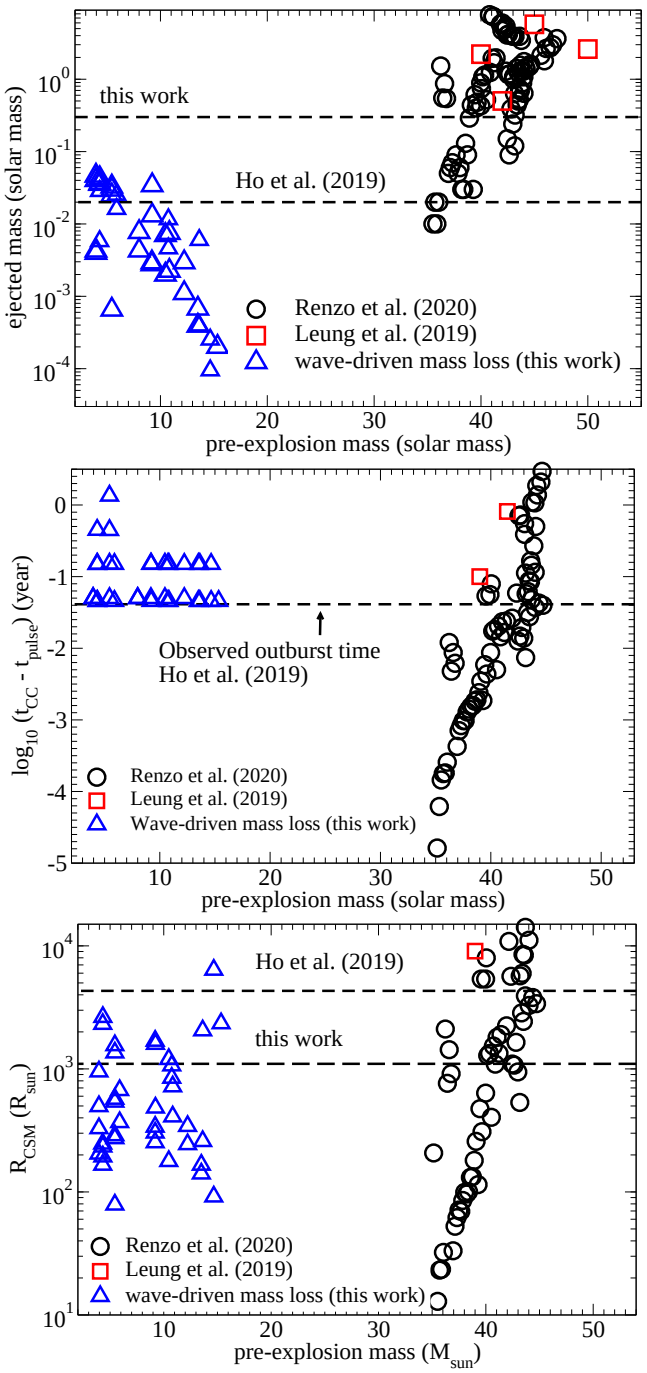

Figure 4. (top panel) A comparison between the CSM properties in the wave-driven mass-loss regime and the pulsational pair-instability supernova regime. Horizontal lines correspond to values derived in Ho et al. (2019) and from our radiative transfer models in Section 4, by using the observed bolometric light curve as a constraint. (middle panel) Same as the top panel but for the time between the mass ejection and core-collapse. (bottom panel) Same as the top panel but for the extracted mass-weighted CSM radius against pre-explosion mass.

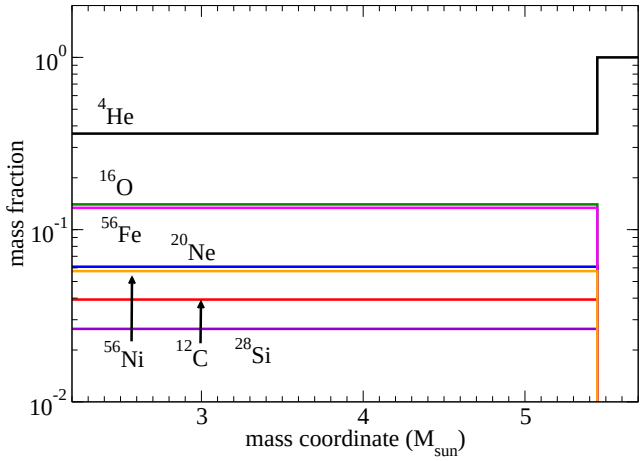

Figure 5. The chemical abundance profile of representative elements used for the benchmark model.

4.1. *Light Curve Modeling*

In this section, we use radiative transfer modeling to derive constraints for the CSM based on the observational data of SN 2018gep. We use the supernova explosion code (Morozova et al. 2015, SNEC) to compute the post-explosion light curve. This code follows the prototype presented in Bersten et al. (2011, 2013). The code has been widely used in the literature so we refer the reader to the instrumentation paper about the detailed implementation and its test cases. Here we only briefly review the our input.

After constructing ordinary stellar evolutionary models (i.e., models without any wave heating), we extract the density and chemical composition profile from MESA. Then we determine some input parameters necessary for SNEC. This includes, 1. the inner mass cut $M_{\rm cut}$, 2. the explosion energy $E_{\rm exp}$ 3. the ^{56}Ni distribution inside the star $X(^{56}{\rm Ni})$. The minimum mass cut is the mass coordinate of the Fe-core, assuming the Fe-core to be promptly collapsing due to gravitational instability. A larger mass-cut corresponds to an explosion with fallback or an aspherical explosion.

For ease of model comparison, we do not use the exact progenitor models from Section 2. Instead, we add parameterized CSM to our models, with properties motivated by wave-driven and pulsation driven mass loss. Outside the original stellar surface, we add a CSM that extends to radius $R_{\rm CSM}$ with mass $M_{\rm CSM}$. The CSM is initially isothermal with a density dependence $\rho \propto 1/r^2$. Similar to Leung et al. (2020b), we assume the ejecta is uniformly mixed. In Figure 5 we plot the chemical abundance of the benchmark model for illustration.

4.2. *Best-fit Model*

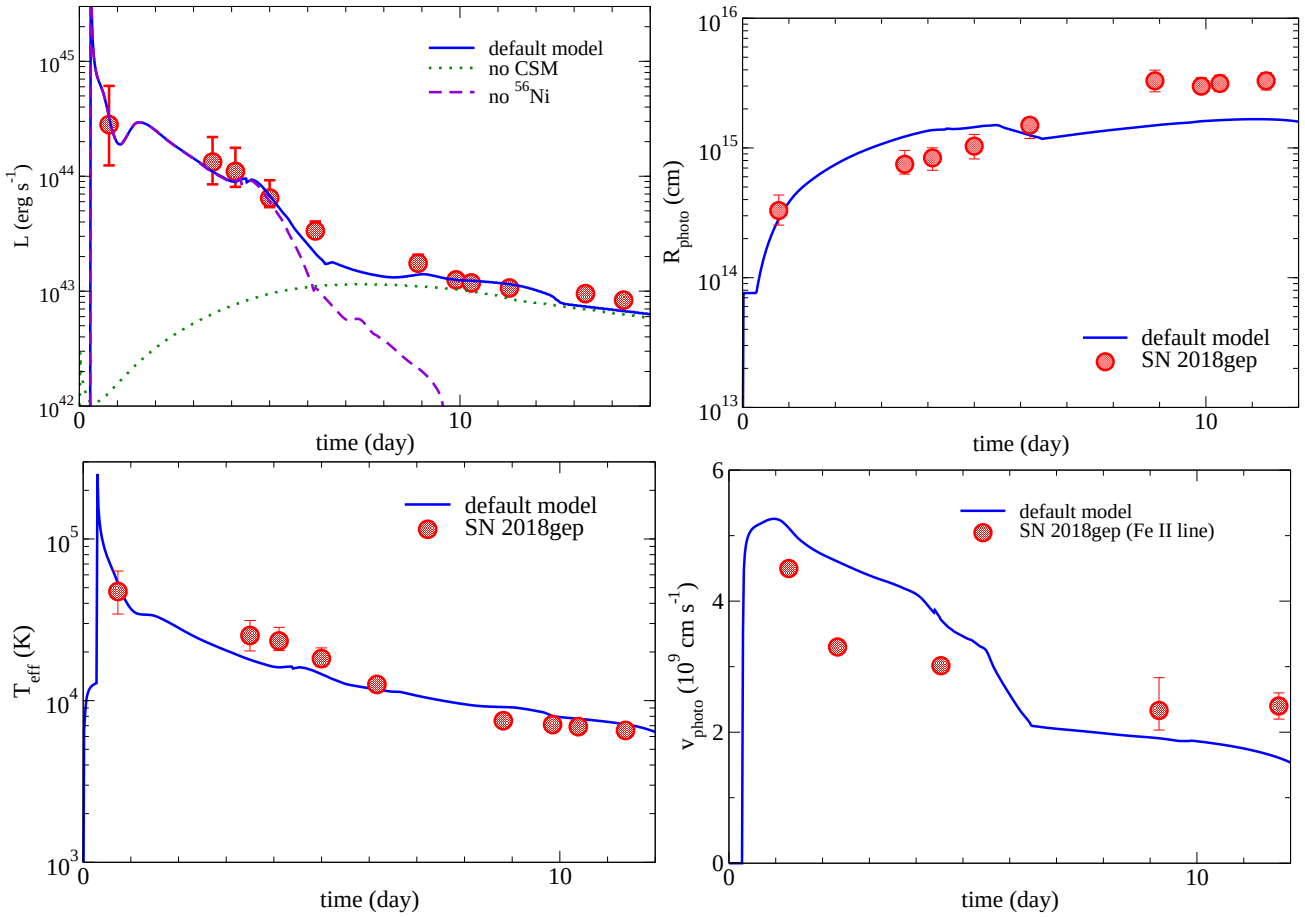

Figure 6. (top left) The light curve of the default model (blue solid line), a contrasting model with only CSM (purple dashed line) or only ^{56}Ni (green dotted line). The red circles correspond to the observed values from SN 2018gep (Ho et al. 2019). (top right) The photosphere radius of the default model. (bottom left) The effective temperature of the default model. (bottom right) The photosphere velocity of the default model.

First we present our default model, which fits many of the features in the bolometric light curve of SN 2018gep. To find a good match, we need to search over progenitor mass M, ejecta mass $M_{\rm ej}$, CSM mass $M_{\rm CSM}$, CSM radius $R_{\rm CSM}$, explosion energy $E_{\rm exp}$, and ^{56}Ni mass in the ejecta $M(^{56}{\rm Ni})$. In such a high dimensional parameter space, we do not attempt to fit the light curve perfectly. Instead, we try to understand how the light curve shape depends on each of the parameters. Table 2 lists the parameters of our default model.

In Figure 6, we plot the bolometric light curve (top left), photospheric radius (top right), effective temperature (bottom left) and photospheric velocity (bottom right) of our default model. For the bolometric light curves, we also include control experiments to demonstrate how the ^{56}Ni-decay (green dotted line) and the pure CSM interaction (purple dashed line) contribute individually to the formation of the full light curve (blue solid line). SN 2018gep shows a two-component structure in the light curve. In the first several days, there is a plateau in the light curve where the luminosity is $\sim 10^{44}$ erg s^{-1}. During this time, the luminosity is almost entirely created by thermal diffusion out of the shock-heated CSM. Around day 5, the CSM contribution decreases rapidly as the CSM becomes optically thin. The light curve falls more steeply until it flattens again when ^{56}Ni-decay dominates the luminosity.

Table 2. The parameters of our default progenitor and explosion model for SN 2018gep.

parameter	value
pre-explosion mass ($M_{\rm fin}$)	5.4 $M_\odot$
explosion energy ($E_{\rm exp}$)	1×10^{52} erg
Ejecta mass ($M_{\rm ej}$)	2.0 $M_\odot$
CSM mass ($M_{\rm CSM}$)	0.3 $M_\odot$
CSM radius ($R_{\rm CSM}$)	1100 $R_\odot$
Nickel mass ($M(^{56}{\rm Ni})$)	0.33 $M_\odot$
CSM slope	-2

In this work, we define $t = 0$ as the moment of explosion of the model, which takes place at UT 2018 September 8 20:20. This is about 0.3 days before the definition of $t = 0$ in Ho et al. (2019) based on the g-band light curve brightening. Indeed, shock breakout occurs roughly 0.3 days after explosion in our default model, roughly consistent with the observed time of rapid brightening.

The observed photospheric radius $R_{\rm ph}$ of SN 2018gep shows a steady rise from an initially high value of $\sim 3 \times 10^{14}$ to $\sim 3 \times 10^{15}$ cm. Our models show similar evolution, albeit with a more rapid initial increase in $R_{\rm ph}$ and a less rapid late-time increase in $R_{\rm ph}$. After day 5, there is a small but sudden drop in $R_{\rm ph}$ in our models when the shock-heated CSM becomes transparent. For the effective temperature $T_{\rm eff}$, the default model follows the trend of SN 2018gep fairly well. The model drops from $\sim 10^5$ K on day 1 to $\sim 10^4$ K at day 6, falling more gradually at later times. The largest discrepancy appears to be at the points between day 3 – 6, where our model under-predicts the temperature and over-predicts the photospheric radius. The imperfect fit could also indicate a CSM with slightly larger radial extent or different density structure could better match the data.

We note the small bumps in the light curve around day 1.5 and day 4.5. These bumps correspond to short temperature plateaus at the photosphere which occur at the first and second recombination of helium. The nearly constant photospheric temperature but increasing photospheric radius creates small and brief increases in the bolometric luminosity.

Lastly, we examine the evolution of the photospheric velocity, which is defined in the models as the Lagrangian velocity at the photosphere. The observed velocities of Ho et al. (2019) are measured using the C/O lines at early times (which are difficult to measure) and the Fe-II line at late times, which typically forms at smaller optical depth (and hence larger velocity) than the blackbody photosphere (Morozova et al. 2020). At most times, the model velocities are within ∼20% of those observed. The model photosphere expands at a very high velocity of $\sim 3-4\times10^9$ cm s^{-1} at early times when it is located within the CSM, but it falls sharply to about 2×10^9 cm s^{-1} when the CSM becomes optically thin. This sharp drop is not apparent in the data, though the sparseness and large uncertainties of the data prevents a detailed comparison.

4.3. *Hydrodynamical Evolution*

We now study how the CSM shock cooling takes place in the default model by examining the evolving hydrodynamical structure. Figure 7 shows the density (top left), temperature (top right), velocity (middle left), the opacity (middle right), the free electron fraction (bottom left), and optical depth (bottom right) at several times after the explosion. Note that the innermost ejecta layers have a mass coordinate of 3.4 $M_\odot$ due to the mass cut used in this model. The initial density profile is that of the stellar model and the constant density CSM. When the shock hits the CSM, it creates a density bump at the contact discontinuity, which gradually vanishes as the star expands. Afterward, the density decreases steadily due to nearly homologous expansion, apart from another density bump that develops near the middle of the ejecta after day 3 at $M(r) \sim 4.3\ M_\odot$. This is produced by a reverse shock propagating inwards from the contact discontinuity with the CSM. The compression associated with the reverse shock creates a density bump. The reverse shock evidently dies out at $M(r) \sim 4.3\ M_\odot$, but the density bump is sustained long afterward.

As expected, the velocity increases with mass coordinate, and the star reaches locally homologous expansion by day 1. Before that, at day 0.01 and 0.1, we capture the moment when the shock hits the CSM and propagates through it. The majority of matter in the progenitor star (up to 5.4 $M_\odot$) expands with a velocity $\sim 2\times10^9$ cm s^{-1}, while the low-density CSM obtains much larger velocities of $3-4\times10^9$ cm s^{-1}. The extremely thin layer of outer CSM can reach as high as 10^{10} cm s^{-1}.

Like the density, temperature generally decreases with time due to (initially adiabatic) expansion. The early shock-CSM collision leads to a hot outer layer of $T > 10^5$ K at early times. A temperature bump propagates inward due to the reverse shock propagating through the inner ejecta, which weakens as the star expands. At late times, the ejecta approaches isothermality as it becomes optically thin.

The opacity profile is closely linked to the temperature profile. After shock heating, the opacity rises by a factor of 2 – 3 where the shock-heated CSM is the most opaque. The opacity is typically largest where the temperature is $\sim 10^5$ K and free-free absorption dominates. At much larger temperatures, electron scattering dominates the opacity and $\kappa \approx 0.2\,{\rm cm}^2/{\rm g}$ for the hydrogen-free ejecta. At much smaller temperatures ($T \lesssim 10^4$ K), the ejecta recombines and the opacity plummets. This occurs starting around day 5, after which the free electron fraction and opacity decrease sharply.

Finally we examine the optical depth evolution in the bottom right panel of Figure 7, where the horizontal line at $\tau = 2/3$ defines the photosphere. In the first 3 days, the photosphere lies in the outermost layers because the shocked heated CSM is opaque. After day 3, the shocked

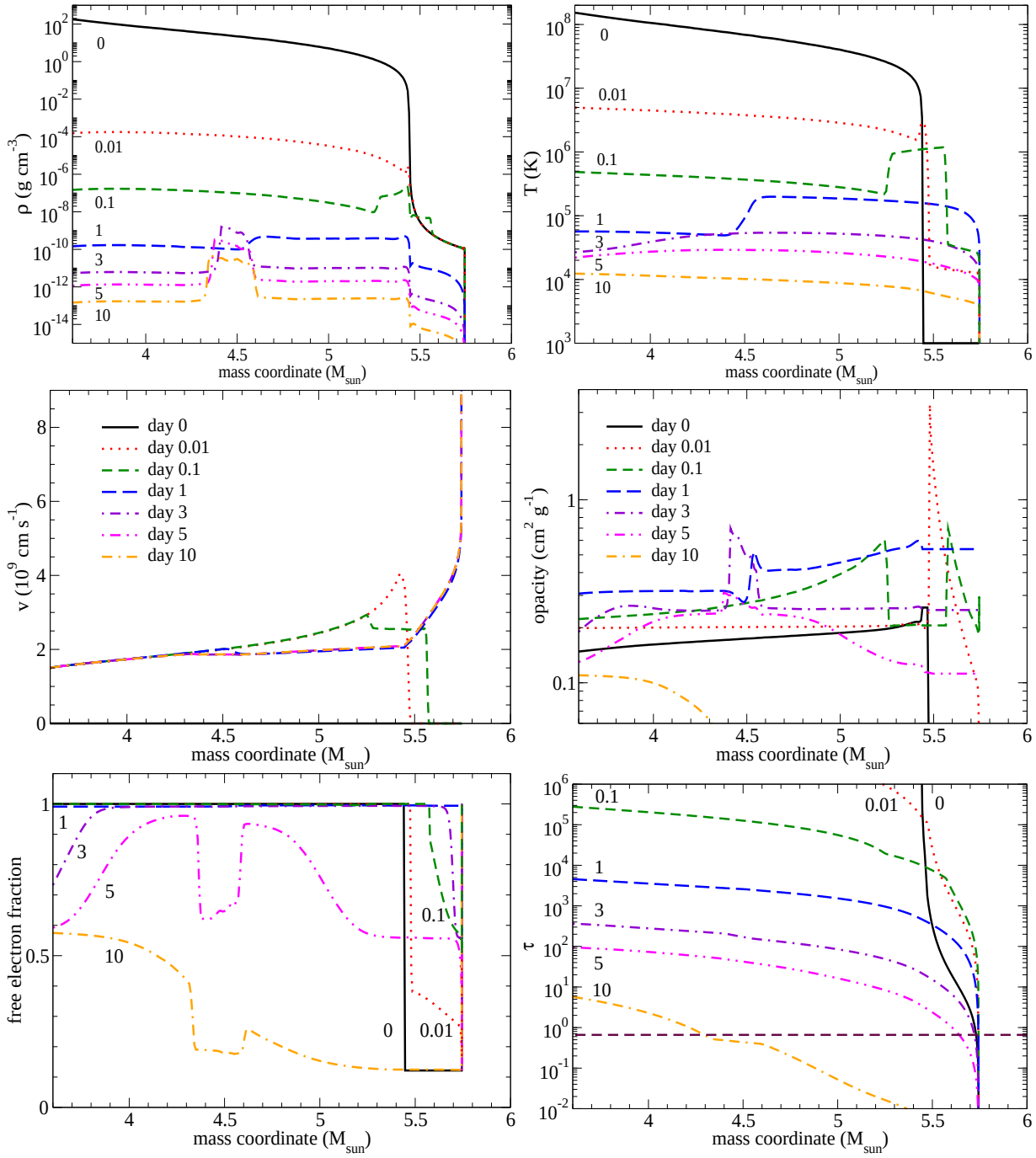

Figure 7. Hydrodynamical evolution of the default model including density (top left), temperature (top right), velocity (middle left), opacity (middle right), free electron fraction (bottom left), and optical depth (bottom right) at day 0 (black solid), 0.01 (red dotted), 0.1 (green dashed), 1 (blue long-dashed), 3 (purple dot-dashed), 10 (magenta dot-dot-dashed) and 15 (orange dot-dash-dashed) respectively. In the optical depth plot, we also add a horizontal line $\tau = 2/3$ whose intersection with the profiles defines the location of the photosphere.

CSM cools and begins to recombine. This causes the optical depth to decrease rapidly such that the photosphere recedes, consistent with the sudden drop of photospheric radius on day 7 in Figure 6. By day 10, the photosphere has receded into the stellar ejecta below the CSM, and by day 15 nearly all of the ejecta is optically thin.

4.4. *Parameter-Dependence of Light Curve Models*

In this section, we examine how parameter variations away from the default model affect the shape of the light curve.

4.4.1. *Dependence on Explosion Energy*

The first parameter we examine is the explosion energy. Because SN 2018gep was a broad-lined Ic SN, the explosion was likely powered by energy sources such as a rapidly rotating magnetar or accretion onto a black hole, which can power an explosion with an energy of order 10^{52} erg. In Figure 8, we plot the SN light curve for models with different explosion energies. The explosion energy has greater importance in the shock-cooling phase (before day 6), where we expect the emergent luminosity to scale linearly with the explosion energy (see Section 5.2), $L_p \propto E_{\rm exp}$. It is less important in the radioactive decay phase (after day 6) where the luminosity is determined primarily by the ^{56}Ni mass. The duration of the shock cooling phase also matches expectations, scaling approximately as $t_p \propto E_{\rm exp}^{-1/4}$ (Section 5.2) due to the faster expansion of the ejecta that shortens the photon diffusion time

4.4.2. *Dependence on CSM Mass*

The CSM mass and structure depends on the progenitor's mass loss mechanism, which is discussed in previous sections. In Figure 8, we plot light curves for models with a few values of $M_{\rm CSM}$, but with the same CSM radius and density profile. We see that when $M_{\rm CSM}$ decreases, the plateau of the light curve remains at nearly constant luminosity but becomes narrower, with duration scaling approximately as $t_p \sim t_d \propto M_{\rm CSM}^{1/2}$ (Section 5.2). This occurs because the shock-heated CSM loses its energy more rapidly due to the shorter photon diffusion time of a lower-mass CSM. All four light curves become similar beyond day 20, where the core ^{56}Ni-decay dominates the energy production process. As discussed above, small CSM masses of $\lesssim 0.1\ M_\odot$ struggle to reproduce the light curve because they produce far too short of a plateau, at least for the CSM structure and radius of our default model.

4.4.3. *Dependence on CSM Radius*

Another important parameter is the CSM radius $R_{\rm CSM}$, which depends primarily on the CSM expansion

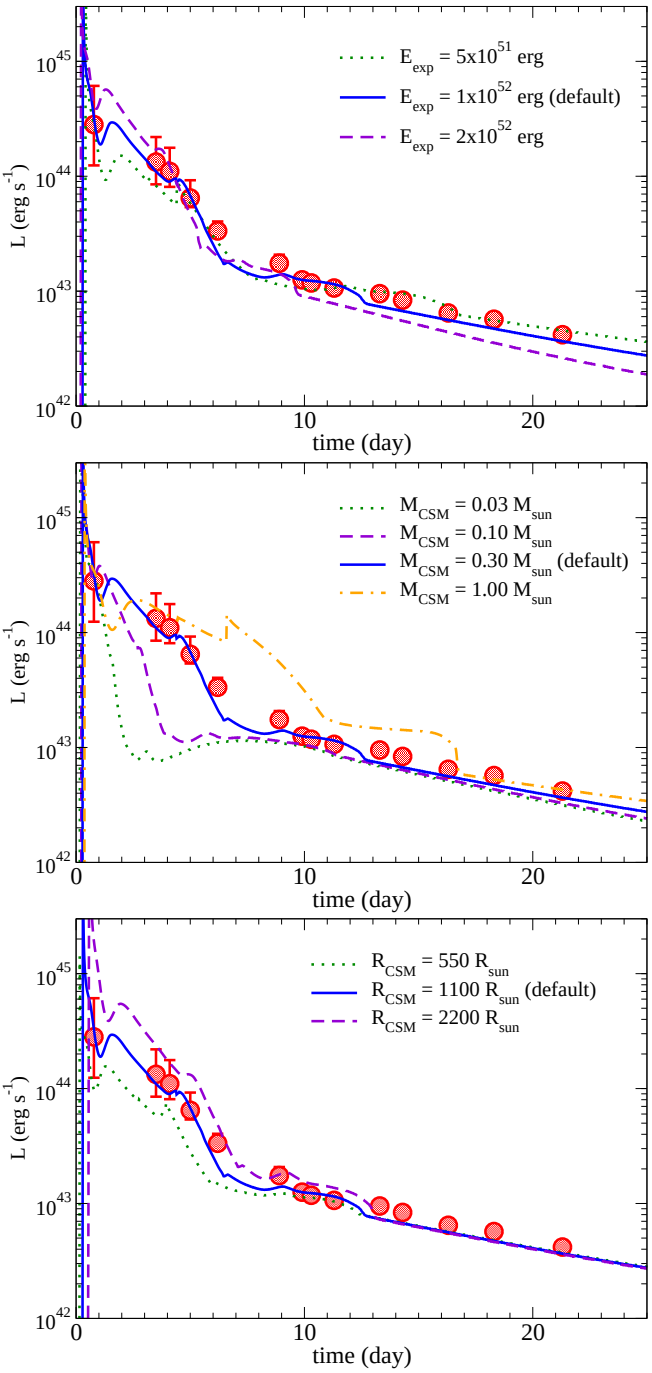

Figure 8. (top panel) Bolometric light curves for the default model (blue solid line) and two comparison models with 5×10^{51} erg (green dotted line) and 2×10^{52} erg (purple dashed line) respectively. (middle panel) Same as the top panel but for models including the default model and three comparison models with $M_{\rm CSM} = 0.03\ M_\odot$ (green dotted line), $0.10\ M_\odot$ (purple dashed line) and $1.00\ M_\odot$ (orange dot-dash line). (bottom panel) Same as the top panel but for models including the default model and comparison models with $R_{\rm CSM} = 550\ R_\odot$ (green dotted line) and $2200\ R_\odot$ (purple dashed line).

velocity and the time delay between the final mass loss and the explosion. In Figure 8, we plot the light curves for models with half and double the CSM radius of the default model. We see that the CSM radius also strongly affects the early time light curve, with larger CSM radii producing brighter plateaus that scale approximately as $L_p \propto R_{\rm CSM}$ (Section 5.2). Larger CSM radii also translate to slightly longer plateau times t_p, even though this is not clearly predicted from analytic models.

4.4.4. *Dependence on ^{56}Ni Mass*

We next examine how the ^{56}Ni mass affects the light curve structure. In Figure 9, we compare the default light curve with models containing no ^{56}Ni or two times more. The zero ^{56}Ni model is identical to that in Figure 6. Again, the early time light curves are essentially identical in all three cases, demonstrating that the ^{56}Ni and ^{56}Co decay do not contribute appreciably to the early time evolution of the light curve. On the other hand, the amount of ^{56}Ni determines the luminosity of the late-time light curve, similar to normal Type Ib/c SNe.

4.4.5. *Dependence on Ejecta Mass*

The total ejecta mass also affects the light curve. In Figure 9, we compare the default models with two other choices of $M_{\rm ej}$. For a lower ejecta mass but the same explosion energy, the ejecta has a larger velocity and becomes optically thin sooner. At the low ejecta masses and high explosion energies considered here, the photon diffusion time is short, such that the width and luminosity of the Ni-powered portion of the light curve is not very sensitive to the ejecta mass, as long as the Ni-decay power is thermalized (which is assumed by our SNEC models). However, we still see that higher ejecta masses stay optically thick for longer, leading to a slower decline at late times relative to low ejecta masses.

4.4.6. *Dependence on CSM Density Profile*

Lastly, we examine how the light curve depends on the slope of the CSM. In Figure 9 we plot the light curve of our default model with a contrasting model in which $\rho_{\rm CSM}$ is constant, but with the same CSM mass and outer radius. We observe that the constant CSM model creates a slightly more extended plateau during the shock cooling phase and the drop of luminosity is slightly slower during the transition towards the ^{56}Ni-decay phase. Beyond day 15, the two models are identical.

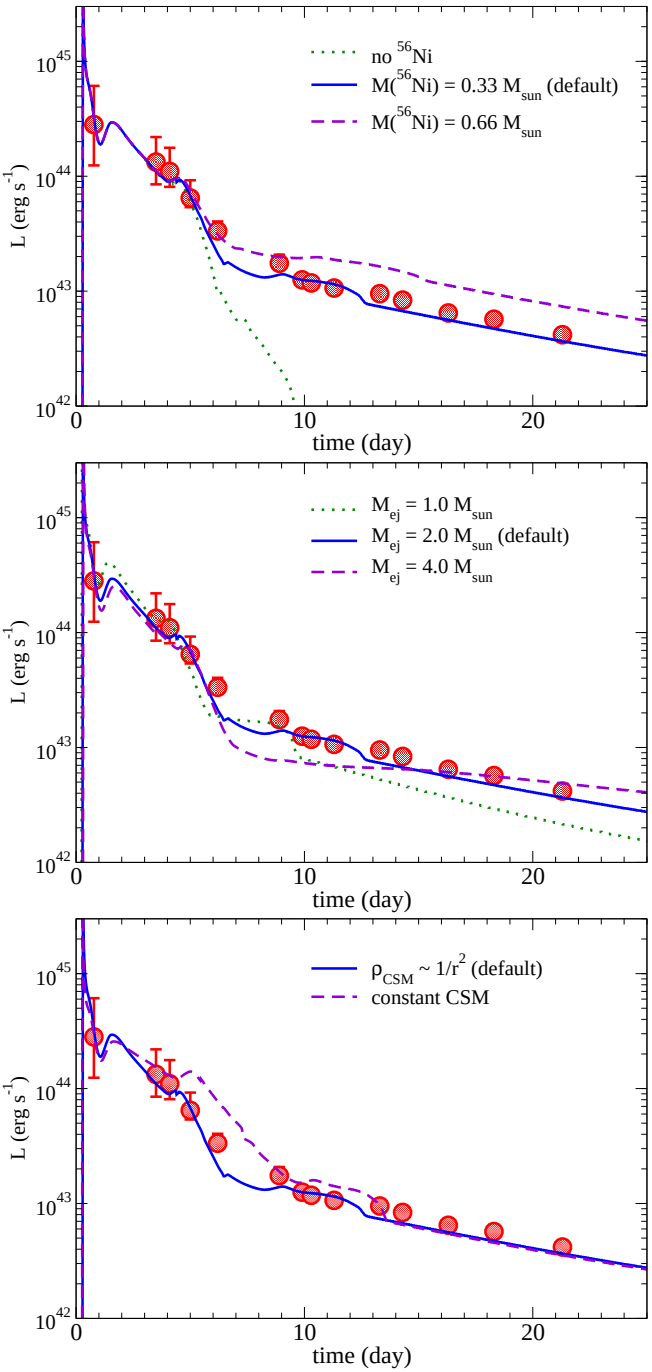

Figure 9. (top panel) Bolometric light curves for the default model (blue solid line) and two comparison models without (green dotted line) and with 0.66 $M_\odot$ (purple dashed line) radioactive ^{56}Ni. (middle panel) Same as the top panel but for models including the default model and two comparison models with ejecta mass $M_{\rm ej}$ = 1.0 $M_\odot$ (green dotted line) and 4.0 $M_\odot$ (purple dashed line). (bottom panel) Same as the top panel but for models including the default model and a contrasting model with constant CSM density (purple dashed line).

5. DISCUSSION

5.1. *Comparison with Models in the Literature*

Only a couple detailed models have been published for SN 2018gep. Based on the sharp rise and high surface temperature, Ho et al. (2019) argued that an extended shock breakout in a circumstellar medium (CSM) powers the initial peak. Their gray-opacity radiative transfer calculation based on analytic CSM profiles found the light curve could be appoximately reproduced with $M_{\rm ej} = 8\ M_\odot$, explosion energy $E_{\rm ej} = 2 \times 10^{52}$ erg, along with a CSM in a shell with mass $M_{\rm CSM} = 0.02\ M_\odot$ and radius $R_{\rm CSM} = 3 \times 10^{14}$ cm with a small width $\sim 3 \times 10^{13}$ cm. These numbers indicate the possibility that this compact SN Ic-BL has experienced mass loss very shortly before the explosion. The model of Ho et al. (2019) is distinctive from our default model above, as they predict a higher $R_{\rm CSM}$ but a lower $M_{\rm CSM}$. While their explosion energy is also larger, the energy per unit mass is similar, as they find $E_{\rm exp}/M = 2.5 \times 10^{51}$ erg/$M_\odot$ and we find $E_{\rm exp}/M = 3.3 \times 10^{51}$ erg/$M_\odot$.

To attempt to distinguish between the competing models, we repeat the light curve calculation with SNEC, using their values as the model input. We thus choose a higher progenitor mass model (50 $M_\odot$, with a pre-explosion mass $\sim 10\ M_\odot$) such that we can allocate 8 $M_\odot$ of ejecta mass. In Figure 10, we plot the light curve using their derived values as numerical inputs, along with our default model but with a $M_{\rm CSM}$ similar to theirs. After sharp early light curve peaks, all of these models fade much more rapidly than the data because the low-mass CSM becomes optically thin very quickly. The luminosity plateaus after day 10, when ^{56}Ni decay dominates the energy source. We also repeat the experiment with a larger mass $M_{\rm CSM} = 0.04\ M_\odot$, but the light curve still fades too fast.

We suspect the main difference (see discussion below) is that the constant opacity used in Ho et al. (2019) is larger than the temperature-dependent opacity in our models. The use of a constant opacity allows the CSM to remain optically thick even after recombination, which slows down the luminosity drop in an unphysical manner. Another difference between their modeling and ours is the use of a thin shell of CSM, which creates a higher CSM density for a given CSM mass, thus allowing the high luminosity to sustain for a longer time. These model differences also change the interpretation the data between day 1 – 4. In our models, shock cooling of the envelope creates a plateau in the first few days, while the extended shock breakout models of Ho et al. (2019) create a large spike in between the data points at 1 and 3 days. Available photometry during that time seems to indicate a luminosity plateau rather than a spike, favoring our shock cooling model. However, the lack of UV data prevents an accurate bolometric luminosity measurement, so we cannot confidently exclude the extended shock breakout model.

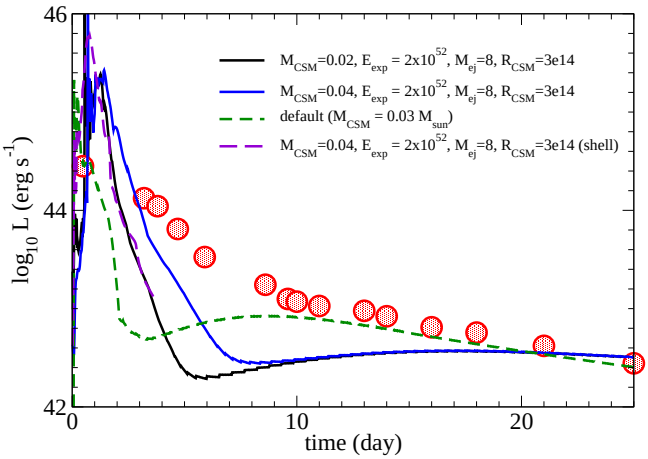

Figure 10. The bolometric light curves predicted by SNEC using the numerical values provided in (Ho et al. 2019) (black line), an identical model with twice as much CSM (blue line), and a comparison using our default model but with a lower CSM mass of 0.03 $M_\odot$ (green dashed line). The observational data for SN 2018gep is shown as as red circles.

Based on fitting multi-colour light curves to semi-analytic models, Pritchard et al. (2020) modeled SN 2018gep as a Type Ib/c supernova with ^{56}Ni-decay power, along with additional power input from a magnetar or CSM-interaction. In their best-fit CSM-interaction model, they derive an ejecta mass 0.49 $M_\odot$, ^{56}Ni mass of 0.13 $M_\odot$, and CSM mass of 0.11 $M_\odot$. Their inferred CSM mass is in between our shock cooling model (0.3 $M_\odot$) and the shock breakout model (0.03 $M_\odot$) from Ho et al. (2019). However, their ejecta mass is significantly smaller than our default model ($\sim 2\ M_\odot$) and that from Ho et al. (2019) (8 $M_\odot$), as is their ^{56}Ni mass. Since Pritchard et al. (2020) does not list an explosion energy or CSM radius, it is unclear which type of shock-interaction powers their models. Their best-fit constant opacity of $\kappa = 0.58\,{\rm cm^2 g^{-1}}$ is likely unphysically large based on the opacities from our more realistic models (Figure 7). Their best-fit magnetar model has a strikingly small ejecta mass 0.26 $M_\odot$ and unphysically large opacity $\kappa = 0.71\,{\rm cm^2 g^{-1}}$. Also, the large fraction of ^{56}Ni in their model challenges the explosion picture; namely how the explosion ejects such a small amount of total mass but such a large amount of ^{56}Ni. For these reasons, we believe our CSM-interaction models are closer to the actual characteristics of SN 2018gep.

5.2. *Comparison with Analytic Model*

For an early light curve is dominated by shock cooling of the extended CSM, our models reveal clear trends in

terms of light curve plateau luminosity, L_p, duration t_p, and slope. Here we compare with the scalings predicted by analytic models (Piro et al. 2020). The asymptotic ejecta speed (Matzner & McKee 1999) is

$$v_t \sim \left(\frac{E_{\rm exp}}{m(r)}\right)^{1/2} \left(\frac{m(r)}{\rho r^3}\right)^{\beta}, \quad (4)$$

with $m(r)$ the enclosed mass, and $\beta \simeq 0.19$. Our models are characterized by a radially extended but low-mass CSM with $M_{\rm CSM} \ll M_{\rm ej}$. Hence, within the CSM, $m(r) \simeq M_{\rm ej}$ and $\rho r^3 \sim M_{\rm CSM}$, such that the CSM ejecta velocity is roughly

$$v_t \sim E_{\rm exp}^{1/2} M_{\rm ej}^{\beta-1/2} M_{\rm CSM}^{-\beta}. \quad (5)$$

The duration of the shock cooling light curve is determined by the diffusion timescale t_d of photons out of the shocked CSM,

$$t_d \sim \left[\frac{\kappa M_{\rm CSM}}{v_t c}\right]^{1/2}, \quad (6)$$

where κ is the opacity. At early times ($t \lesssim t_d$), the luminosity evolves as

$$L(t) \sim \frac{c R_{\rm CSM} v_t^2}{\kappa} \left(\frac{t_d}{t}\right)^{4/(n-2)}, \quad (7)$$

The luminosity and photospheric radius fall sharply after a time scale

$$t_{\rm ph} \sim \left[\frac{\kappa M_{\rm CSM}}{v_t^2}\right]^{1/2}. \quad (8)$$

In the constant opacity approximation, the plateau luminosity is therefore expected to scale approximately as $L_p \propto R_{\rm CSM} E_{\rm exp} M_{\rm CSM}^{-2\beta} M_{\rm ej}^{2\beta-1}$. The light curve will drop sharply after a plateau duration $t_{\rm ph} \propto E_{\rm exp}^{-1/2} M_{\rm CSM}^{1/2+\beta} M_{\rm ej}^{1/2-\beta}$. Hence, for a constant plateau luminosity and duration, we expect $R_{\rm CSM} \propto M_{\rm CSM}^{-1}$ and $E_{\rm exp} \propto M_{\rm CSM}^{1+2\beta} M_{\rm ej}^{1-2\beta}$. The scalings provided above are approximately consistent with the light curve modeling results of the previous sections.

5.3. *Light Curve Degeneracies*

The above analytic relations for the light curve luminosity and plateau duration predict degeneracies between the CSM mass, radius, and explosion energy, as are well known for Type II-P SNe (Goldberg & Bildsten 2020). To understand whether our inferred CSM parameters for SN 2018gep are subject to such degeneracies, we computed additional numerical models which are analytically predicted to have the same plateau luminosity and duration. In Figure 11, we plot the light curves for the default model (solid blue line) and a contrasting model with $2.60\times E_{\rm exp}$, $2\times M_{\rm CSM}$ and $0.5\times R_{\rm CSM}$ (Model 1, purple dashed line), and another with $0.38 \times E_{\rm exp}$, $0.5 \times M_{\rm CSM}$ and $2 \times R_{\rm CSM}$ (Model 2, green dashed line).

We find that the analytic scaling relations work fairly well (though not perfectly) in the parameter range considered, as the numerically computed luminosity, photospheric radius and effective temperature for the three models are similar. The more compact model (Model 1) has a slightly lower peak luminosity and slower fall in luminosity during the shock-cooling phase. Minor deviations from the analytic predictions occur because the differing density and temperature changes the opacity, which affects how the photosphere recedes. These results echo the findings of Dessart & Hillier (2019); Goldberg & Bildsten (2020) for type-II-P supernova light curves, where they showed that the light curve shape allows for degeneracy between the mass and radius of the progenitor's hydrogen envelope.

However, in contrast to Type II-P SNe where the envelope mass dominates the ejecta mass, the inferred CSM mass for SN 2018gep is much smaller than the total ejecta mass. This means the the photospheric velocity scales approximately as $v \propto E_{\rm exp}/M_{\rm ej}$ and is not plagued by the same degeneracy noted by Goldberg & Bildsten (2020) for Type II-P SNe, so the photospheric velocity can potentially be used to break the degeneracy. In this case, a higher $E_{\rm exp}$ (Model 1) leads to a higher photosphere velocity, which predicts photospheric velocities substantially larger than those observed at early times (Figure 11). A better match is obtained for our default model or lower $E_{\rm exp}$ (Model 2). We caution that the measured Fe II line velocity is highly uncertain and is likely to be slightly larger than the continuum photospheric velocity because it is formed farther out in the ejecta (e.g., Paxton et al. 2018). We conclude that the CSM properties likely lie somewhere in between the default model and Model 2, i.e., in the range $0.15\,M_\odot \lesssim M_{\rm CSM} \lesssim 0.3\,M_\odot$, $1100\,R_\odot \lesssim R_{\rm CSM} \lesssim 2200\,R_\odot$, and $5\times10^{51}\,{\rm erg} \lesssim E_{\rm exp} \lesssim 10^{52}\,{\rm erg}$. More detailed modeling should be performed to identify other possible degeneracies (e.g., between $E_{\rm exp}$ and $M_{\rm ej}$, whether these can be broken by the Ni-powered portion of the light curve, and to robustly estimate uncertainties in the inferred explosion parameters.

5.4. *Asphericity and Jet-like Explosion*

The relatively low ejecta mass of our default model is very small compared to the progenitor mass for PPISNe (i.e. progenitor masses of roughly 80 – 140 with pre-explosion masses of roughly 35 – 50 $M_\odot$). Hence, adopt-

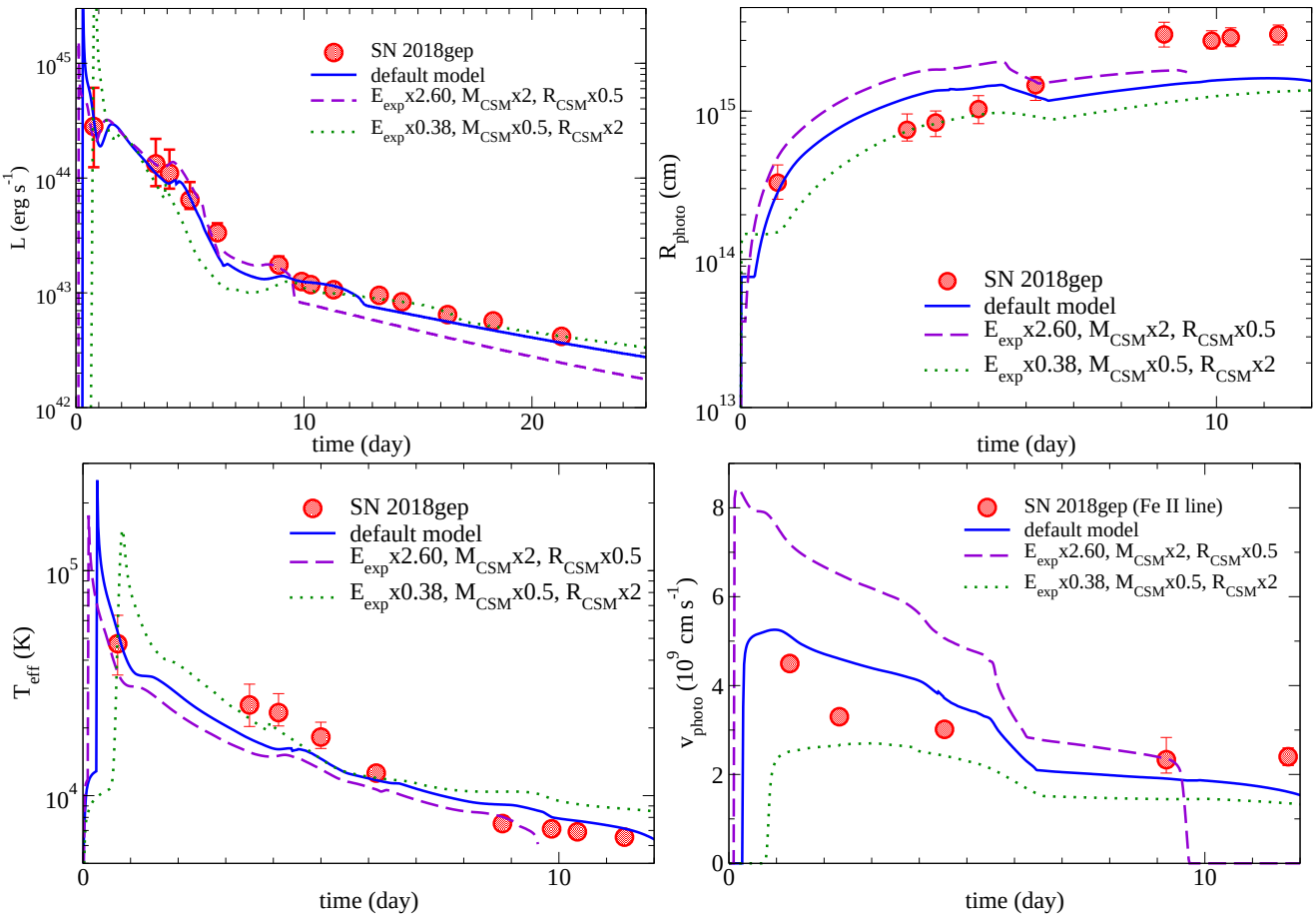

Figure 11. (top left) The bolometric light curve of the default model and the contrasting model with $E_{\rm exp} \times 2.60$, $M_{\rm CSM} \times 2.60$ and $R_{\rm CSM} \times 0.5$ (purple dashed line) and $E_{\rm exp} \times 0.38$, $M_{\rm CSM} \times 0.5$ and $R_{\rm CSM} \times 2$ (green dotted line). (top right) Same as top left panel but for the photosphere radius. (bottom left) Same as top left panel but for the effective temperature. (bottom right) Same as top left panel but for the photosphere velocity.

ing the PPISN interpretation likely requires that the ejecta be highly aspherical (e.g., a bipolar jet-driven outflow) or that nearly all of the star collapses into a black hole and only a small fraction is ejected.

Both of these possibilities may be realized in the collapsar scenario for driving the explosion, in which the explosion energy arises from a jet and/or disc wind from an accreting black hole (Woosley & Heger 2006; Woosley & Bloom 2006). Numerical simulations of collapsars show that the conservation of angular momentum leads to an accretion disk with a standing shock (e.g. Molteni et al. 1996; Stone et al. 1999). The disk can drive an outflow containing a couple solar masses, a few tenths of a solar mass of ^{56}Ni, and an energy of $\sim 10^{52}$ erg (see e.g., MacFadyen & Woosley 1999; Kohri et al. 2005; Zenati et al. 2020), similar to the properties of our default model. Alternatively, the explosion could be driven by a rapidly rotating magnetar (e.g., Obergaulinger & Aloy 2020). The jet (e.g., Maeda et al. 2002; Nagataki et al. 2003; Nomoto et al. 2013) can cause shock heating in the envelope, which creates a distinctive nucleosynthetic pattern including lots of ^{56}Ni (Tominaga 2009). The breakout can lead to a long gamma-ray burst (Tominaga et al. 2007; Nagataki 2011). However, whether the jet breaks out depends strongly on its energetics (Zhang et al. 2008), with a smothered jet resulting in a Type Ic-BL event like SN 2018gep.

One-dimension models of massive stellar explosions (e.g., Heger & Woosley 2010; Nomoto 2017; Limongi & Chieffi 2020), predict that an explosion energy of roughly 2×10^{51} erg is necessary to produce $\sim 0.3\ M_\odot$ of ^{56}Ni in the ejecta, for progenitor models with masses $M \lesssim 20\,M_\odot$. Higher explosion energies of roughly 5×10^{51} erg are required for higher mass stars (Umeda & Nomoto 2008). The low-mass progenitor possibility is roughly consistent with our wave-driven models (though the explosion energy is lower than that inferred from light curve modeling), while the high-mass possibility is more consistent with our PPISN models. In

the low-mass progenitor scenario, the small ejecta mass inferred from light curve modeling is expected from the $\sim 4-5\,M_\odot$ helium core of the progenitor star. In the high-mass progenitor scenario, a small ejecta mass requires asymmetric explosion models in which most of the ^{56}Ni and explosion energy is contained within a small amount of mass, possibly ejected within bipolar jets.

It will be interesting future work to self-consistently model the pre-SN evolution of a rapidly rotating helium star with pre-SN mass of $\approx 40\,M_\odot$. If it can produce pre-SN ejecta of $\sim 0.3\,M_\odot$ due to pulsational pair instability before collapse, and generate a $\sim 10^{52}$ erg explosion with a few solar masses of high-velocity ejecta, it could likely produce an event like SN 2018gep.

6. CONCLUSION

We have simulated the process of wave-driven pre-supernova mass loss in hydrogen-free supernova progenitors, examining the mass loss as a function of the progenitor's pre-explosion mass, the total deposited energy, and the deposition duration. Within the parameter range motivated by detailed stellar evolutionary models, a larger CSM mass can result from a shorter deposition duration (for a fixed energy) or a higher energy deposition (for a fixed duration). Low pre-explosion progenitor masses ($M \lesssim 10\,M_\odot$) appear to be necessary for producing large CSM masses in the range $M_{\rm CSM} \gtrsim 10^{-2}\ M_\odot$, because the specific binding energy is much larger for higher mass helium stars, so the energy budget of the wave heating mechanism is likely not sufficient to eject large amounts of mass.

We also explored the physical origin of the superluminous rapid transient SN 2018gep (Ho et al. 2019), spectroscopically classified as a Type Ic-BL SN. The rapid rise and high peak luminosity is best explained via CSM interaction and shock cooling of the CSM (as opposed to extended shock breakout), providing a constraint on the mass-loss mechanism of the progenitor star prior to its final explosion. By modeling the bolometric light curve, we find a good fit for CSM interaction models with explosion energy $E_{\rm exp} = 1 \times 10^{52}$ erg, CSM mass $M_{\rm CSM} = 0.30\ M_\odot$, CSM radius $R_{\rm CSM} = 1100\ R_\odot$, ejecta mass $M_{\rm ej} = 2.0\ M_\odot$, and nickel mass $M(^{56}{\rm Ni}) = 0.33\,M_\odot$. In this interpretation, the bright early light curve of SN 2018gep is created by shock cooling of the extended CSM, after which the transient evolves into a "normal" nickel-powered Ic-BL SN.

We have extensively tested how the bolometric light curve in the shock-cooling phase and the ^{56}Ni-decay phase of our models depends on the model parameters above. Our results indicate that our fitting is relatively robust, given the large number of free parameters in the models. Like Type II-P SNe, our CSM shock-cooling models do exhibit moderate degeneracy in the light curve shape (peak luminosity and its width) for a given $E_{\rm exp}$, $M_{\rm ej}$, $R_{\rm CSM}$ and $M_{\rm CSM}$. Hence, there could be other combinations of these parameters that provide similarly good fits to the data, so our solution may not be unique.

We show that the interpretation of SN 2018gep could be compatible with two distinct mechanisms: 1. wave-driven mass loss from a fairly low-mass $M \sim 5\,M_\odot$ helium star progenitor, which ejects $M_{\rm CSM} \sim 0.1\,M_\odot$ of CSM to large radii, or 2. pulsational pair instability mass loss of a very massive ($M \sim 40\,M_\odot$) progenitor, which ejects $M_{\rm CSM} \sim 0.3\,M_\odot$) in the final weeks of its life. We favor the latter scenario because wave-driven mass loss struggles to eject enough CSM in the shock-cooling interpretation of the light curve. Addtionally, the high-energy broad-lined nature of the SN suggests the explosion is powered by a rapidly rotating central engine unlikely to form in low-mass SN progenitors. This is also consistent with the low-metallicity environment of SN 2018gep, and with its bright observed outburst roughly two weeks before explosion.

In the pulsational mass loss interpretation of SN 2018gep, the progenitor of this event was a $\approx 40\,M_\odot$ helium star at the boundary between Type Ic SNe and superluminous Type Ic SNe. Slightly lower mass progenitors do not eject enough mass via pulsational pair instability to affect the light curves, producing Type Ic or Ic-BL SNe. Slightly higher mass progenitors eject much more mass to larger radii, potentially producing longer lasting Type Ic superluminous SNe via CSM interaction. Our interpretation of SN 2018gep may help unify these seemingly distinct classes of SNe into one conceptual framework.

7. ACKNOWLEDGMENT

We thank Jared Goldberg, David Khatami, and the ZTF theory network for useful discussions that helped inspire and refine this work. S.C.L thanks the MESA development community for making the code open-sourced and V. Morozova and her collaborators in providing the SNEC code open source. S.C.L. and JF acknowledges support by NASA grants HST-AR-15021.001-A and 80NSSC18K1017. K.N. has been supported by the World Premier International Research Center Initiative (WPI Initiative), MEXT, Japan, and JSPS KAKENHI Grant Numbers JP17K05382 and JP20K04024.

REFERENCES

Barkat, Z., Rakavy, G., & Sack, N. 1967, Phys. Rev. Lett., 18, 379

Bellm, E. C., Kulkarni, S. R., Graham, M. J., et al. 2019, PASP, 131, 018002, doi: 10.1088/1538-3873/aaecbe

Bersten, M. C., Benvenuto, O., & Hamuy, M. 2011, ApJ, 729, 61, doi: 10.1088/0004-637X/729/1/61

Bersten, M. C., Tanaka, M., Tominaga, N., Benvenuto, O. G., & Nomoto, K. 2013, ApJ, 767, 143, doi: 10.1088/0004-637X/767/2/143

Blinnikov, S. 2017, in Handbook of Supernovae, ed. A. W. Alsabti & P. Murdin (Cham: Springer International Publishing AG), 843, doi: 10.1007/978-3-319-21846-5_31

Chatzopoulos, E., Wheeler, J. C., & Couch, S. M. 2013, ApJ, 776, 129, doi: 10.1088/0004-637X/776/2/129

Chevalier, R. A. 1982, ApJ, 258, 790, doi: 10.1086/160126

—. 2012, ApJL, 752, L2, doi: 10.1088/2041-8205/752/1/L2

Dessart, L., & Hillier, D. J. 2019, A&A, 625, A9, doi: 10.1051/0004-6361/201834732

Dexter, J., & Kasen, D. 2013, ApJ, 772, 30, doi: 10.1088/0004-637X/772/1/30

Fuller, J. 2017, MNRAS, 470, 1642, doi: 10.1093/mnras/stx1314

Fuller, J., & Ro, S. 2018, MNRAS, 476, 1853, doi: 10.1093/mnras/sty369

Gilmer, M. S., Kozyreva, A., Hirschi, R., Fröhlich, C., & Yusof, N. 2017, ApJ, 846, 100, doi: 10.3847/1538-4357/aa8461

Goldberg, J. A., & Bildsten, L. 2020, ApJL, 895, L45, doi: 10.3847/2041-8213/ab9300

Graham, M. J., Kulkarni, S. R., Bellm, E. C., et al. 2019, PASP, 131, 078001, doi: 10.1088/1538-3873/ab006c

Heger, A., & Woosley, S. E. 2002, Astrophys. J., 567, 532

Heger, A., & Woosley, S. E. 2010, ApJ, 724, 341, doi: 10.1088/0004-637X/724/1/341

Hirschi, R. 2017, in Handbook of Supernovae, ed. A. W. Alsabti & P. Murdin (Cham: Springer International Publishing AG), 567, doi: 10.1007/978-3-319-21846-5_120

Ho, A. Y. Q., Goldstein, D. A., Schulze, S., et al. 2019, ApJ, 887, 169, doi: 10.3847/1538-4357/ab55ec

Jones, S., Hirschi, R., Nomoto, K., et al. 2013, ApJ, 772, 150, doi: 10.1088/0004-637X/772/2/150

Kasen, D. 2017, in Handbook of Supernovae, ed. A. W. Alsabti & P. Murdin (Cham: Springer International Publishing AG), 939, doi: 10.1007/978-3-319-21846-5_32

Kasen, D., & Bildsten, L. 2010, ApJ, 717, 245, doi: 10.1088/0004-637X/717/1/245

Kasen, D., Metzger, B. D., & Bildsten, L. 2016, ApJ, 821, 36, doi: 10.3847/0004-637X/821/1/36

Kasen, D., Woosley, S. E., & Heger, A. 2011, ApJ, 734, 102, doi: 10.1088/0004-637X/734/2/102

Kohri, K., Narayan, R., & Piran, T. 2005, ApJ, 629, 341, doi: 10.1086/431354

Kuriyama, N., & Shigeyama, T. 2020, arXiv e-prints, arXiv:2006.06389. https://arxiv.org/abs/2006.06389

Leung, S.-C., Blinnikov, S., Ishidoshiro, K., Kozlov, A., & Nomoto, K. 2020a, ApJ, 889, 75, doi: 10.3847/1538-4357/ab6211

Leung, S.-C., Blinnikov, S., Nomoto, K., et al. 2020b, arXiv e-prints, arXiv:2008.11404. https://arxiv.org/abs/2008.11404

Leung, S.-C., & Fuller, J. 2020, ApJ, 900, 99, doi: 10.3847/1538-4357/abac5d

Leung, S.-C., & Nomoto, K. 2019, PASA, 36, e006, doi: 10.1017/pasa.2018.49

Leung, S.-C., Nomoto, K., & Blinnikov, S. 2019, ApJ, 887, 72, doi: 10.3847/1538-4357/ab4fe5

Limongi, M., & Chieffi, A. 2020, ApJ, 902, 95, doi: 10.3847/1538-4357/abb4e8

MacFadyen, A. I., & Woosley, S. E. 1999, ApJ, 524, 262, doi: 10.1086/307790

Maeda, K., Nakamura, T., Nomoto, K., et al. 2002, ApJ, 565, 405, doi: 10.1086/324487

Maeda, K., Tanaka, M., Nomoto, K., et al. 2007, ApJ, 666, 1069, doi: 10.1086/520054

Marchant, P., Renzo, M., Farmer, R., et al. 2019, ApJ, 882, 36, doi: 10.3847/1538-4357/ab3426

Margutti, R., Metzger, B. D., Chornock, R., et al. 2019, ApJ, 872, 18, doi: 10.3847/1538-4357/aafa01

Matzner, C. D., & McKee, C. F. 1999, ApJ, 510, 379, doi: 10.1086/306571

Molteni, D., Ryu, D., & Chakrabarti, S. K. 1996, ApJ, 470, 460, doi: 10.1086/177877

Moriya, T. J., Blinnikov, S. I., Tominaga, N., et al. 2013, MNRAS, 428, 1020, doi: 10.1093/mnras/sts075

Moriya, T. J., Sorokina, E. I., & Chevalier, R. A. 2018, SSRv, 214, 59, doi: 10.1007/s11214-018-0493-6

Moriya, T. J., Tominaga, N., Langer, N., et al. 2014, A&A, 569, A57, doi: 10.1051/0004-6361/201424264

Morozova, V., Piro, A. L., Fuller, J., & Van Dyk, S. D. 2020, ApJL, 891, L32, doi: 10.3847/2041-8213/ab77c8

Morozova, V., Piro, A. L., Renzo, M., et al. 2015, ApJ, 814, 63, doi: 10.1088/0004-637X/814/1/63

Nagataki, S. 2011, PASJ, 63, 1243, doi: 10.1093/pasj/63.6.1243

Nagataki, S., Mizuta, A., Yamada, S., Takabe, H., & Sato, K. 2003, ApJ, 596, 401, doi: 10.1086/377530

Nomoto, K. 2017, in Handbook of Supernovae, ed. A. W. Alsabti & P. Murdin (Cham: Springer International Publishing AG), 1931, doi: 10.1007/978-3-319-21846-5_86
Nomoto, K., Kobayashi, C., & Tominaga, N. 2013, ARA&A, 51, 457, doi: 10.1146/annurev-astro-082812-140956
Nomoto, K., & Leung, S.-C. 2017, in Handbook of Supernovae, ed. A. W. Alsabti & P. Murdin (Cham: Springer International Publishing), 1–39, doi: 10.1007/978-3-319-20794-0_62-1
Obergaulinger, M., & Aloy, M.-Á. 2020, arXiv e-prints, arXiv:2008.07205. https://arxiv.org/abs/2008.07205
Ohkubo, T., Nomoto, K., Umeda, H., Yoshida, N., & Tsuruta, S. 2009, ApJ, 706, 1184, doi: 10.1088/0004-637X/706/2/1184
Ouchi, R., & Maeda, K. 2019, ApJ, 877, 92, doi: 10.3847/1538-4357/ab1a37
Paxton, B., Bildsten, L., Dotter, A., et al. 2011, Astrophys. J. Suppl., 192, 3
Paxton, B., Cantiello, M., Arras, P., et al. 2013, ApJS, 208, 4
Paxton, B., Marchant, P., Schwab, J., et al. 2015, ApJS, 220, 15
Paxton, B., Schwab, J., Bauer, E. V., et al. 2017, ApJS, 234, 34
Paxton, B., Schwab, J., Bauer, E. B., et al. 2018, ApJS, 234, 34, doi: 10.3847/1538-4365/aaa5a8
Perley, D. A., Mazzali, P. A., Yan, L., et al. 2019, MNRAS, 484, 1031, doi: 10.1093/mnras/sty3420
Piro, A. L., Haynie, A., & Yao, Y. 2020, arXiv e-prints, arXiv:2007.08543. https://arxiv.org/abs/2007.08543
Prentice, S. J., Maguire, K., Smartt, S. J., et al. 2018, ApJL, 865, L3, doi: 10.3847/2041-8213/aadd90
Pritchard, T. A., Bensch, K., Modjaz, M., et al. 2020, arXiv e-prints, arXiv:2008.04321. https://arxiv.org/abs/2008.04321
Quataert, E., & Shiode, J. 2012, MNRAS, 423, L92, doi: 10.1111/j.1745-3933.2012.01264.x
Renzo, M., Farmer, R., Justham, S., et al. 2020, A&A, 640, A56, doi: 10.1051/0004-6361/202037710
Schrøder, S. L., MacLeod, M., Loeb, A., Vigna-Gómez, A., & Mandel, I. 2020, ApJ, 892, 13, doi: 10.3847/1538-4357/ab7014
Shiode, J. H., & Quataert, E. 2014, ApJ, 780, 96, doi: 10.1088/0004-637X/780/1/96
Smartt, S. J., Clark, P., Smith, K. W., et al. 2018, The Astronomer's Telegram, 11727, 1
Smith, N. 2017, in Handbook of Supernovae, ed. A. W. Alsabti & P. Murdin (Cham: Springer International Publishing AG), 403, doi: 10.1007/978-3-319-21846-5_38
Sorokina, E., Blinnikov, S., Nomoto, K., Quimby, R., & Tolstov, A. 2016, ApJ, 829, 17, doi: 10.3847/0004-637X/829/1/17
Stone, J. M., Pringle, J. E., & Begelman, M. C. 1999, MNRAS, 310, 1002, doi: 10.1046/j.1365-8711.1999.03024.x
Tolstov, A., Nomoto, K., Blinnikov, S., et al. 2017, Astrophys. J., 835, 266
Tolstov, A., Nomoto, K., Sorokina, E., et al. 2019, ApJ, 881, 35, doi: 10.3847/1538-4357/ab2876
Tominaga, N. 2009, ApJ, 690, 526, doi: 10.1088/0004-637X/690/1/526
Tominaga, N., Umeda, H., & Nomoto, K. 2007, ApJ, 660, 516, doi: 10.1086/513063
Umeda, H., & Nomoto, K. 2002, ApJ, 565, 385, doi: 10.1086/323946
—. 2003, Nature, 422, 871, doi: 10.1038/nature01571
—. 2008, ApJ, 673, 1014, doi: 10.1086/524767
Wang, L. J., Wang, X. F., Wang, S. Q., et al. 2018, ApJ, 865, 95, doi: 10.3847/1538-4357/aadba4
Wang, L. J., Wang, X. F., Cano, Z., et al. 2019, MNRAS, 489, 1110, doi: 10.1093/mnras/stz2184
Wang, S.-Q., & Li, L. 2020, ApJ, 900, 83, doi: 10.3847/1538-4357/aba6e9
Whitesides, L., Lunnan, R., Kasliwal, M. M., et al. 2017, ApJ, 851, 107, doi: 10.3847/1538-4357/aa99de
Woosley, S. E. 2010, ApJL, 719, L204, doi: 10.1088/2041-8205/719/2/L204
Woosley, S. E. 2017, ApJ, 836, 244
Woosley, S. E. 2018, ApJ, 863, 105, doi: 10.3847/1538-4357/aad044
—. 2019, ApJ, 878, 49, doi: 10.3847/1538-4357/ab1b41
Woosley, S. E., Blinnikov, S., & Heger, A. 2007, Nature, 450, 390
Woosley, S. E., & Bloom, J. S. 2006, ARA&A, 44, 507, doi: 10.1146/annurev.astro.43.072103.150558
Woosley, S. E., & Heger, A. 2006, ApJ, 637, 914, doi: 10.1086/498500
Wu, S., & Fuller, J. 2020, arXiv e-prints, arXiv:2011.05453. https://arxiv.org/abs/2011.05453
Yoshida, T., Umeda, H., Maeda, K., & Ishii, T. 2016, MNRAS, 457, 351, doi: 10.1093/mnras/stv3002
Zenati, Y., Siegel, D. M., Metzger, B. D., & Perets, H. B. 2020, MNRAS, 499, 4097, doi: 10.1093/mnras/staa3002
Zhang, W., Woosley, S. E., & Heger, A. 2008, ApJ, 679, 639, doi: 10.1086/526404